Rock physics constrained anisotropic WEMVA: Part II - Field data test

Yunyue (Elita) Li, Robert Clapp, Biondo Biondi, and Dave Nichols

ABSTRACT

We test our rock physics constrained anisotropic WEMVA methodology on a Gulf of Mexico dataset. Based on the well logs and the previously inverted lithological interpretations, we perform stochastic rock physics modeling to sample the possible ranges of the anisotropic parameters. These modeling results are then summarized by an average model and a cross-parameter covariance matrix under the multivariate Gaussian assumption. When inverting the surface seismic data using the anisotropic WEMVA method, we start from the average model and regularize the inversion using the geological dips and the cross-parameter covariance. The preliminary results show improvements in the migrated image with higher resolution and better definition of the dipping sedimentary layers around the salt in the shallow region. Further iterations are needed to better resolve the VTI model and to properly focus the image at depth.

INTRODUCTION

Earth model building is an underdetermined and hence challenging inverse problem, especially at the exploration stage. In general, the input information can be obtained from geological information, surface seismic data, and rock physics modeling from well logs. During early exploration, the geological information often comes from plate or regional tectonics to identify the potential target area. Surface seismic data are acquired to image the structure of the subsurface after establishing the area of interest. Based on the preliminary interpretation results, a few exploration wells will be drilled to verify the earth model. The initial model building results are often far from the true subsurface. Therefore, corrections of the earth model by integrating all available information are necessary.

Surface seismic data have the best compromise between accuracy and coverage among the three types of information. Geological knowledge covers large regions without specific positions, whereas well logs provide accurate, high resolution information only at sparse locations. Therefore, most of the current practices of information integration occur after seismic imaging and structural interpretation. First, seismic images are stretched vertically according to the well markers. Then, borehole core analysis is propagated from the well location to the rest of the region based on the seismic images and the underlying geological assumptions. However, this conventional workflow does not include a feedback loop to verify if the modified seismic

images honor the original seismic data. Therefore, inconsistencies may be introduced by the sequential evaluations of the data.

In this study, we examine a surface seismic dataset which was acquired offshore Gulf of Mexico (GoM) by Schlumberger Multiclient. Migration images based on isotropic Earth models are obtained from the seismic data and the reservoir properties are interpreted based on the well logs following a conventional data integration workflow. However, both the well logs and the lithological interpretations suggest that the sedimentary basin consists of large portion of shales, which contradicts the isotropic Earth assumption during seismic imaging. Furthermore, the migration image manifests steep dips in both in-line and cross-line directions where the sediments were pulled up by the salt intrusion. Wavepaths reflected from these structures can be highly sensitive to the anisotropic parameters. Consequently, the inconsistencies in the isotropic Earth model may lead to defocused image and/or incorrect positioning of the reflectors.

To take advantage of the complementary information in all data, we propose to integrate geological and rock physics information during the seismic inversion when building an anisotropic Earth model. As introduced by the companion paper (Li et al., 2014), we include the geological information as dip filters and rock physics information as cross-parameter covariances. By evaluating all objectives at the same time, we hope to resolve an anisotropic Earth model which is consistent with all the available data.

Another challenge of the field application is the large computational cost associated with the large volume of data. We take advantage of the redundancy of the data when computing the gradient by randomly removing two thirds of all shots in each iteration. We show that the gradients obtained by the reduced number of shots contain the same update information with limited under-stacked noise and unbalance effects. These artifacts can be further suppressed by changing the random set of shots through WEMVA iterations.

The structure of this paper contains two parts. In the first part, we perform stochastic rock physics modeling based on the well log measurements and the interpretation results output from a previous seismic processing workflow. This exercise enables us to explore the possible range of the anisotropic models. We obtain the background (averaged) anisotropic model to initialize the WEMVA inversion and the cross-parameter covariance matrix to regularize the inversion.

In the second part, we invert a subset of the 3-D GoM seismic data based on the model and the constraints from the stochastic rock physics modeling. Preliminary results show improvements in the migrated image with higher resolution and better definition of the sedimentary structure around the salt in the shallow region. Further iterations are needed to better resolve the VTI model and to properly focus the image at depth.

STOCHASTIC ROCK PHYSICS MODELING FOR SHALE ANISOTROPY

Many rock physics models have been proposed to describe shale anisotropy, considering both the intrinsic mineral anisotropy and the particle alignment during compaction. In this paper, we combine the rock physics models proposed by Bachrach (2010) and Bandyopadhyay (2009). We model a sedimentary rock using two distinctive components: the anisotropic shale component and the isotropic sand component. We model the shale anisotropy from three aspects: mineral anisotropy of the constituents of the rock, compaction effect on the particle alignment, and the transition from smectite to illite due to compaction and temperature. We model the sand as pure quartz. To combine the sand component with the shale component, we consider two different models: the suspension model which models sand (quartz) as inclusions in the shale background, and the lamination model which models sand and shale as a laminated system.

We refer the readers to the details of the rock physics modeling in a previous paper (Li et al., 2013). The process of rock physics modeling for shale anisotropy is summarized in the following workflow (Algorithm 1). Between different realization of the rock physics modeling, the key parameters for the modeling are varied in a range determined by the well log measurements. Therefore, assembly of models, instead of a single model are obtained. These models are the source of the prior rock physics covariance.

Algorithm 1 Stochastic rock physics modeling workflow

for $n = 1 \cdots N_{\text{real}}$ **do**
  Initialize the modeling parameters.
  Compute the percentage of illite in the rock given a temperature model.
  Compute the average stiffness coefficients for smectite and illite, given a porosity model.
  Compute the volumetric percentage for each of the mineral phase, given a volumetric percentage of shale.
  Compute the effective stiffness coefficients using suspension model and lamination model.
  Compute the VTI models from the effective stiffness coefficients.
end for

To perform the modeling, we need the following inputs: a temperature model, a porosity model and a shale content model. We assume the temperature model is smooth and it can be approximated using a typical temperature gradient in the GoM. We use the provided shale content inversion cube (Figure 1(a)) and modeled a smoothly varying porosity trend (Figure 1(b)) from the provided P-wave velocity. The high shale content estimates indicate that the subsurface is rich in clay minerals at all depths. The shale content slightly increases with depth. The low porosity region below 5km in Figure 1(b) highlights a shale-rich basin between the salt bodies.

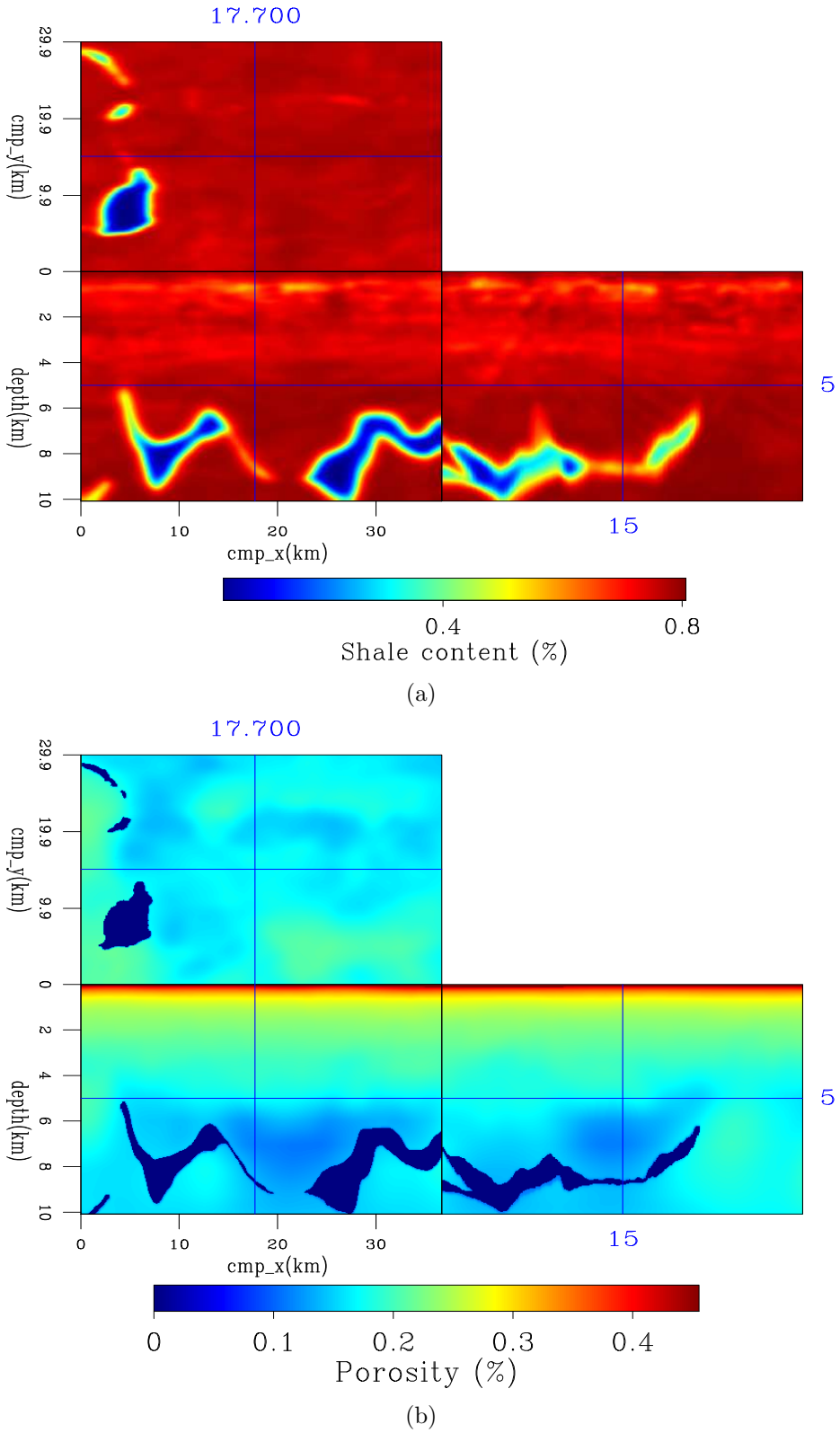

(a)

(b)

Figure 1: Interpreted shale content (a) and modeled porosity (b). [**ER**]

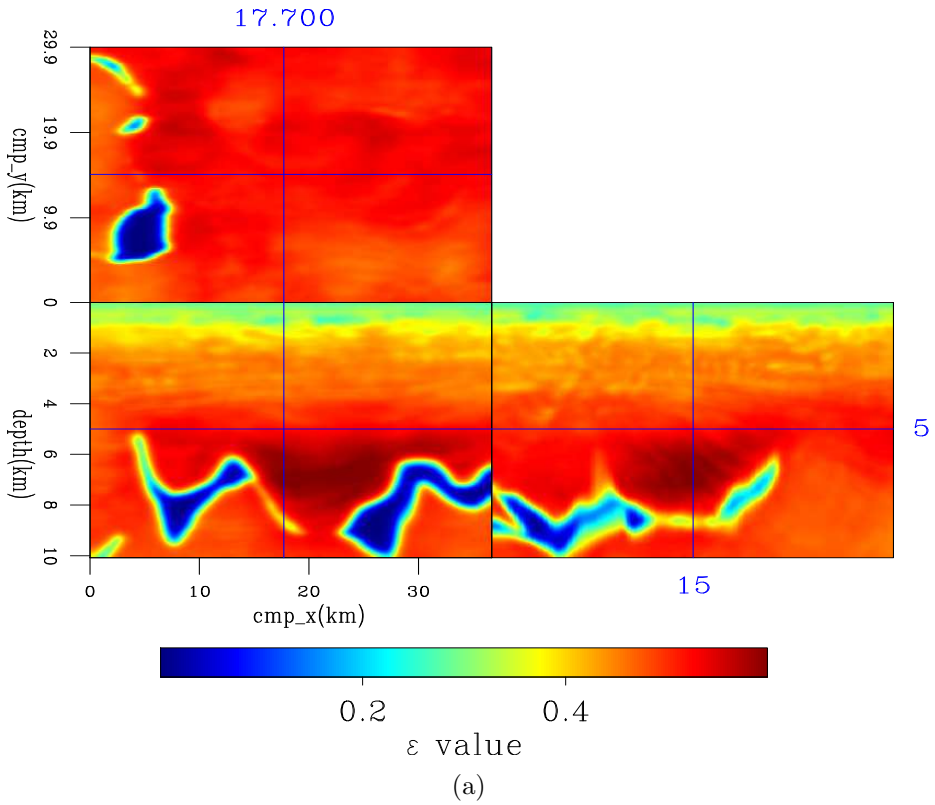

(a)

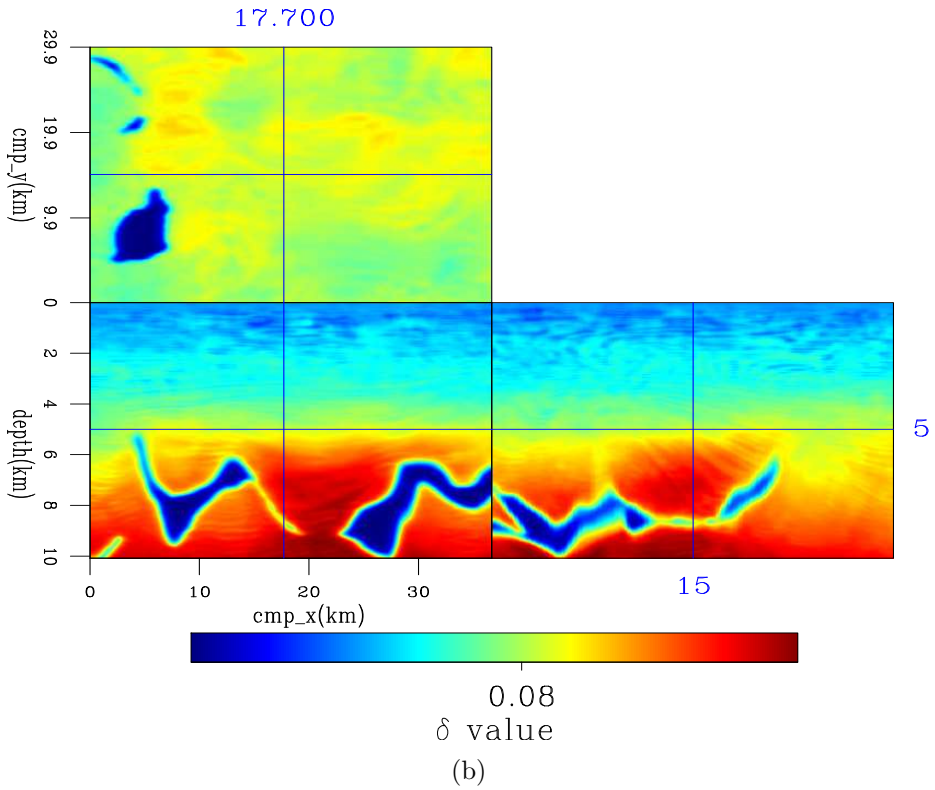

(b)

Figure 2: Average ϵ model (a) and average δ model (b). Both are obtained from the stochastic rock physics modeling experiment. [**ER**]

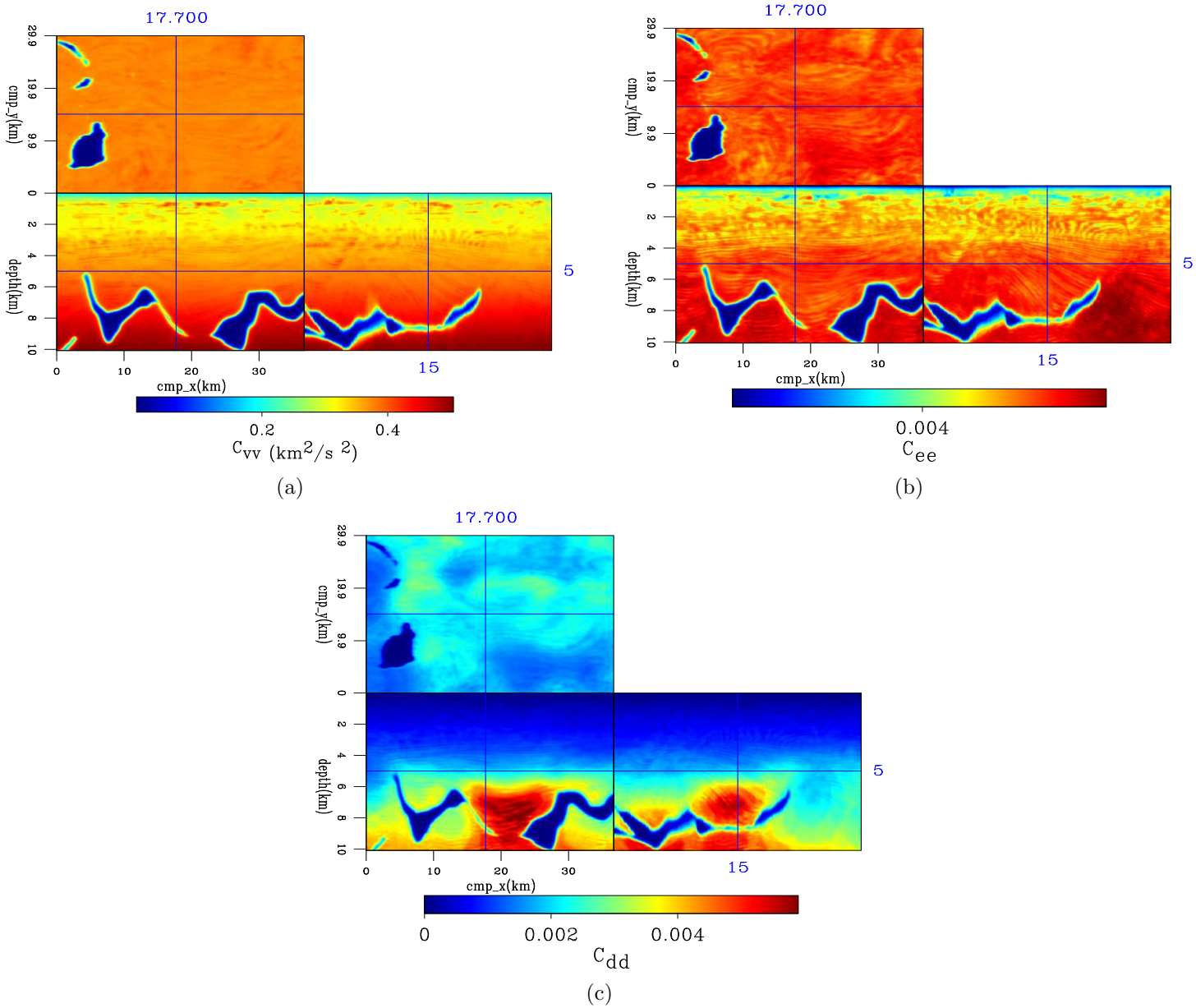

Figure 3: Diagonal elements of the covariance matrix. (a): Variance of vertical velocity; (b): Variance of ϵ; and (c): Variance of δ. [**ER**]

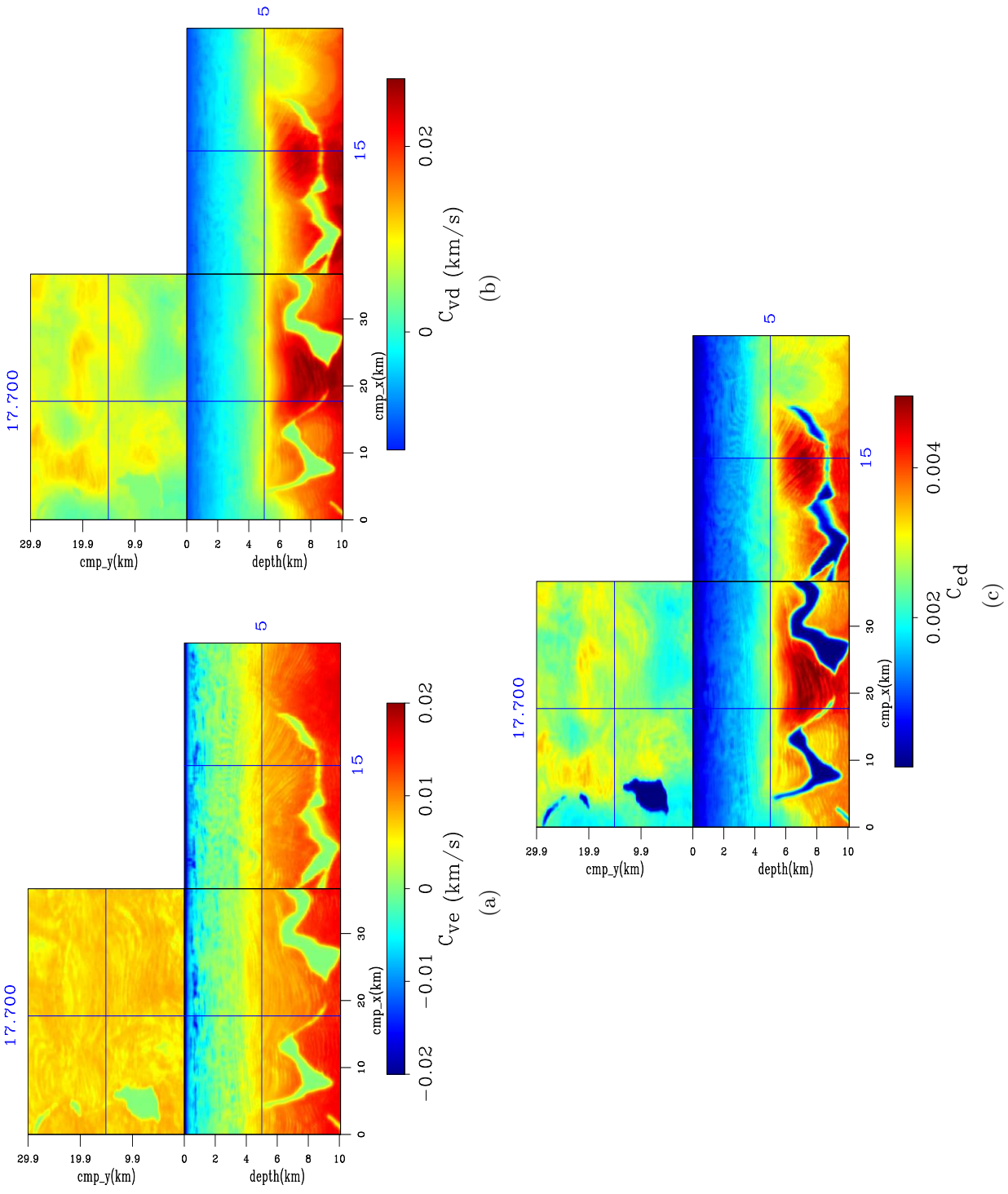

Figure 4: Off-diagonal elements of the covariance matrix. (a): Covariance between vertical velocity and ϵ; (b): Covariance between vertical velocity and δ; and (c): Covariance between ϵ and δ. [**ER**]

Figure 2 shows an example of the ϵ and δ model from the rock physics modeling. The maximum resolution of the modeled anisotropic models is similar to the resolution of the interpreted shale content. Nonetheless, users can control the resolution of the anisotropic models by smoothing the modeling results. Note that given the chosen rock physics model, both anisotropic parameters ϵ and δ are correlated with the shale content and are inversely correlated with the porosity.

More importantly than producing a single modeling result, the stochastic rock physics modeling also allows us to explore the possible ranges of the anisotropic parameters. By varying the key parameters of the rock physics model, we explore different initial compaction states, different compaction rates, different temperature gradients, as well as different temperature windows for smectite-to-illite transition. As a result, we obtain multiple realizations of the anisotropic model at each subsurface location.

Assuming the three parameters v_v, ϵ, and δ follow a multivariate Gaussian distribution, we summarize their variance with a 3×3 matrix where only 6 elements are independent. Figure 3 shows the diagonal elements in the covariance matrix. The variance of the vertical velocity (Figure 3(a)) has an increasing trend with respect to depth. There is no strong correlation between the variance in velocity and the lithology. The ϵ variance (Figure 3(b)) and the δ variance (Figure 3(c)) show more spatial variations than the variance of velocity.

Figure 4 shows the off-diagonal elements in the covariance matrix. The cross-covariance map between v_0 and ϵ (Figure 4(a)) suggests these two parameters are negatively correlated in the shallow region but positively correlated in the deep region. This velocity-anisotropy correlation can be explained by rock properties. In the shallow region, high velocity correlates with low anisotropic sand; whereas in the deeper region, high velocity can be caused by mineral diagensis from smectite to illite, which is also highly anisotropic (Vernik and Liu, 1997). Covariance between ϵ and δ (Figure 4(c)) shows positive correlations for all depths.

ANISOTROPIC WEMVA ON 3-D FIELD DATA IN THE GULF OF MEXICO

The most important piece of information of the subsurface comes from the seismic data. In this section, we discuss the preprocessing and the inversion of the seismic data to build reliable anisotropic models.

Acquisition and preprocessing

The seismic data were acquired offshore Louisiana in the Gulf of Mexico (Figure 5). Seismic data were collected using sensors laid out along ocean bottom cables (OBC). The source lines are orthogonal to the receiver cables.

We work with a subset of the 3-D dataset due to the limited computation resources. Figure 6 shows the source and receiver locations of the study area given by the cross-spread geometry. The sources are spaced 400 m in-line and 50 cross-line (with respect to the receiver lines). The receivers are spaced 50 m in-line and 600 m cross-line. Due to the relatively sparse locations for the receivers, we use reciprocity to exchange the sources and receivers.

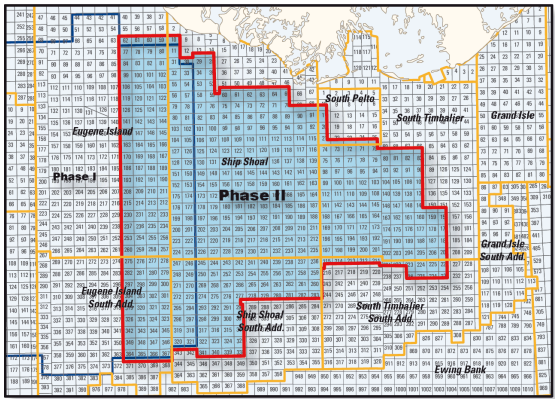

Figure 5: Area covered by the E-Dragon Phase II acquisition. Ocean bottom cables were laid out on the sea bed under shallow water with an average depth of 120 m. [**NR**]

We group the receivers onto a 50×600 grid and the sources onto a 50×50 grid. Figure 7 shows the acquisition pattern for a single receiver. Figure 8(a) shows the receiver gather corresponding to the acquisition geometry in Figure 7. In the in-line direction, large acquisition holes are consistent with the sparse in-line source sampling. In the better sampled cross-line direction, we notice strong dispersive arrivals with high amplitudes after 3.5s. These low frequency surface wave events dominate the receiver gather in the later time.

To remove the surface waves, we apply a bandpass filter to select the reflection energy between 3Hz and 25Hz. The upper bound of the frequency band is limited by the available computational resources. We also apply a first arrival muting and a $t^{2.5}$ time weighting on the receiver gather to boost up the later arrivals. The receiver gather after preprocessing is shown in Figure 8(b). We treat the receiver gather as a shot gather and use the implicit finite different implementation of the one-way wave-equation (Shan, 2008) to perform shot-profile migration.

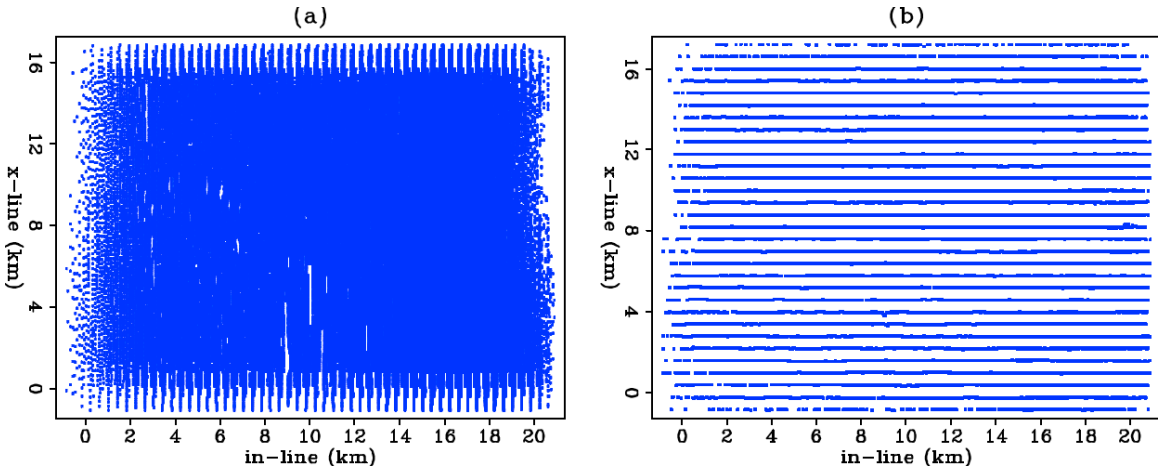

Figure 6: Cross-spread geometry of the GoM dataset. Panel (a): Source locations; Panel (b): Receiver locations. Notice the source lines and the receiver lines are perpendicular to each other. We call the direction along the receiver line the in-line direction and the perpendicular direction cross-line direction. [**ER**]

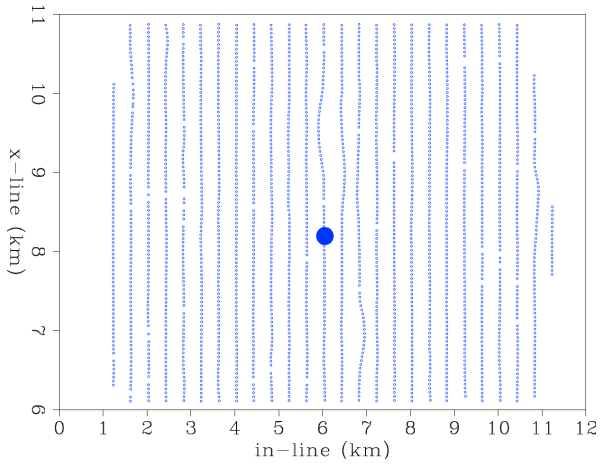

Figure 7: Acquisition pattern for one particular receiver. Source locations are denoted by "o" and the receiver location is denoted as the solid circle. For any given receiver, the maximum in-line offset is about 6km and the maximum cross-line offset is about 3km. [**ER**]

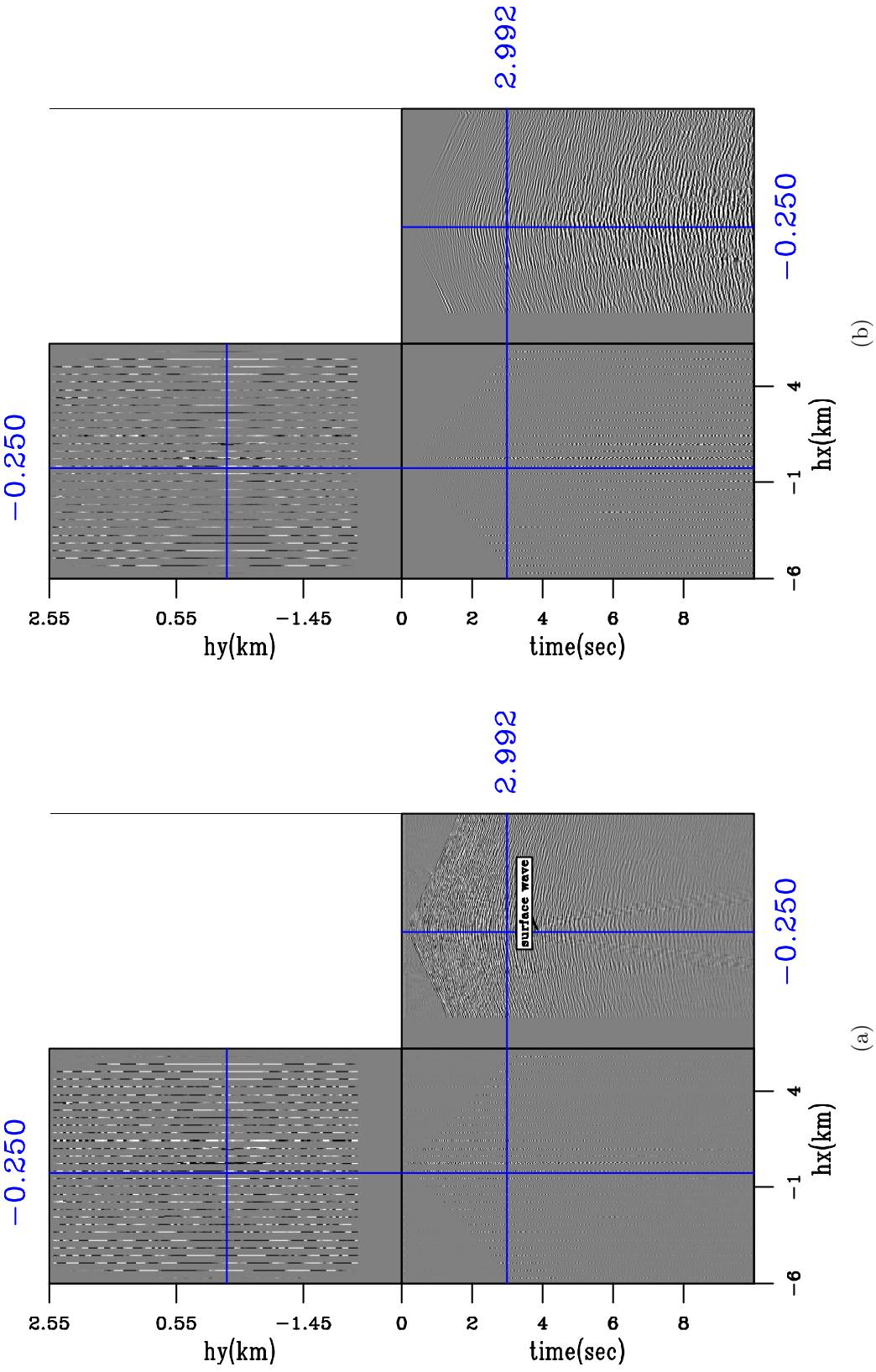

Figure 8: (a): One receiver gather shows the dense cross-line sampling and very coarse in-line sampling. The slow arrivals after 3.5s are the low frequency surface wave events. (b): Same receiver gather after bandpass, muting, and time weighting. Notice the surface waves are attenuated and the reflection events in the later time are more visible. [**ER**]

Initial anisotropic model and gradients

An initial ray-based tomography has been performed by Schlumberger. Figure 9(a) shows the provided isotropic velocity model. Figures 9(b) to 9(d) show the initial anisotropic model. The initial ϵ model (Figure 9(c)) and δ model (Figure 9(d)) are the averaged models from the stochastic rock physics modeling. The salt body and the water column are considered isotropic. We assume that the tomographic isotropic velocity (Figure 9(a)) best estimates the NMO velocity in a VTI parameterization. Therefore, we compute the anisotropic vertical velocity model 9(b) from the δ model (Figure 9(d)) and the isotropic NMO velocity (Figure 9(a)). The vertical velocity is slightly smaller than the NMO velocity thanks to a positive δ model.

Figure 10(a) and Figure 11(a) compare the isotropic migration image at two different locations with the anisotropic migration image in Figure 10(b) and Figure 11(b), respectively. Compared with Figure 10(a), the depths of the flat reflectors in the anisotropic migration image (Figure 10(b)) remain roughly the same thanks to a small δ value. Nevertheless, the focusing of these shallow flat events are improved by the anisotropic model. The depth slice of the anisotropic migration image shows better coherence and higher resolution on the discontinuities across the fault (labeled 1 and 2). The dipping reflectors in the in-line direction (highlighted by oval) and the strong near-horizontal reflector above 6km (labeled 3) in the cross-line direction are also more continuous in the anisotropic migration image. Comparison between Figure 11(a) and Figure 11(b) shows similar qualities in both migration images. The crossing events and broken reflectors below 4km in the cross-line direction indicate better models are needed to properly focus the image.

To update the anisotropic model, we propose to use anisotropic wave-equation migration velocity analysis (WEMVA) (Li and Biondi, 2011). The anisotropic WEMVA objective function reads as follows:

$$S(\mathbf{m}) = -\frac{1}{2}||\sum_{\theta}\mathbf{I}(\mathbf{x},\theta)|| + \alpha\frac{1}{2}(\mathbf{m}-\mathbf{m}_{\text{prior}})^T\mathbf{C}_M^{-1}(\mathbf{m}-\mathbf{m}_{\text{prior}}), \tag{1}$$

where the first term defines the "data fitting" objective by maximizing the stacking power, and the second term defines the "model regularization" objective by including the geological and the rock physics information through the initial model $\mathbf{m}_{\text{prior}}$ and the covariance matrix $\mathbf{C}_M$. Parameter α balances the relative weights between the two objectives.

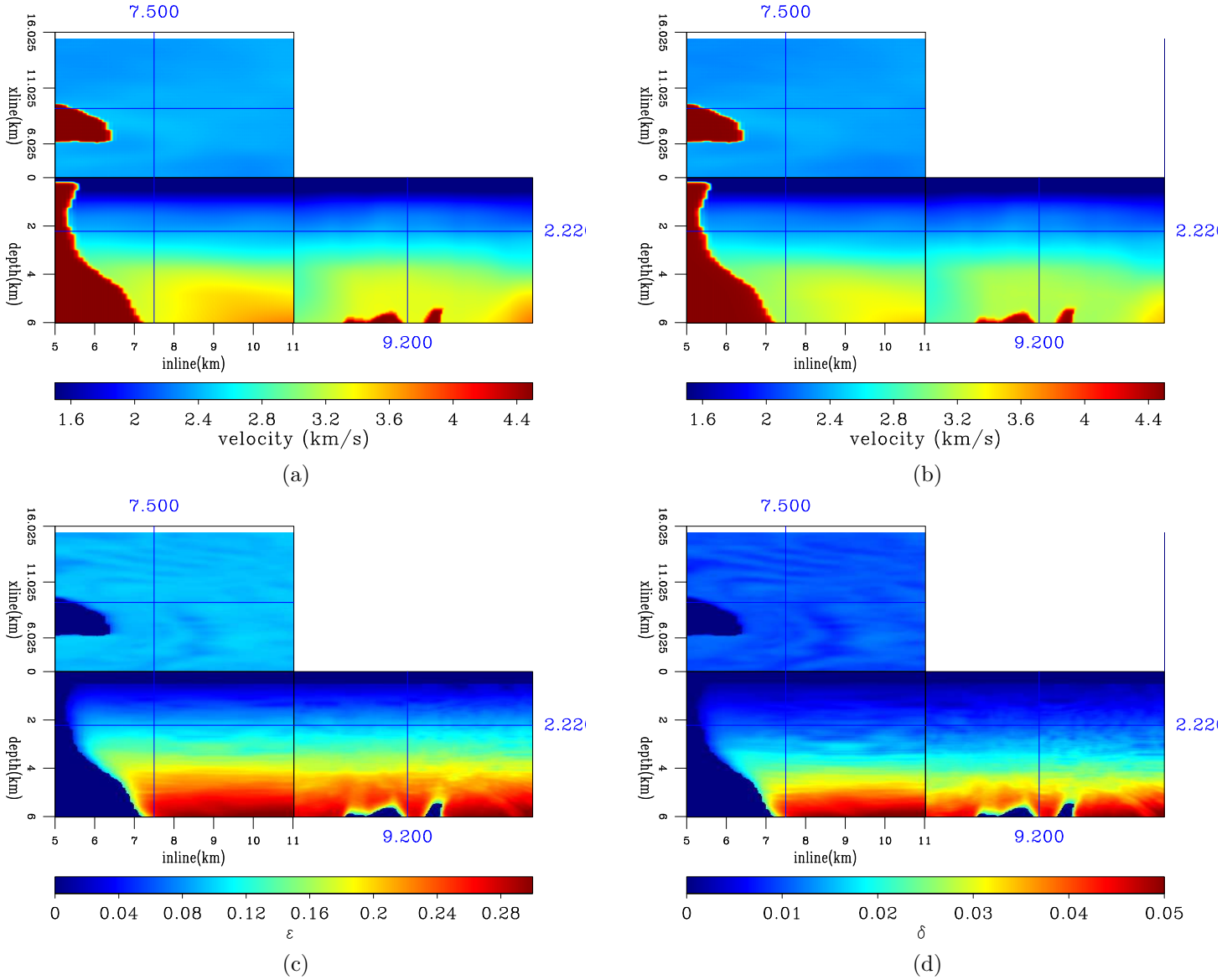

Figure 9: (a): Isotropic velocity model provided by ray-based tomography. (b): Vertical velocity model, (c): initial ϵ model and (d): initial δ model from the rock physics modeling. [**CR**]

Each anisotropic WEMVA iteration has three main computation-intensive steps: migration, gradient computation, and the line search process which usually involves a few migration/function evaluations. We summarize the computational cost during each anisotropic WEMVA iteration in Table 1. Computation time for each process is measured on a single node with OpenMP parallelization over 16 processors. Assuming 60 nodes are always available, it takes 56 hours to finish one WEMVA iteration.

Table 1 shows that the most expensive step in WEMVA is the gradient computation. To reduce the computation cost, we take advantage of the redundancy in shots when computing the gradient. During each iteration, we randomly choose one-third of the shots to perform the tomographic gradient calculations. The inaccuracy introduced by the subsampling is insignificant because the gradient updates are usually smooth and it is incoherent with the inaccuracies in the next iterations when another set of random shots are used. Therefore, the stacking of the updates over iterations will also suppress the artifacts in the gradients.

Note that the subsampling strategy is not applied for the migration and the line search steps, although it would greatly reduce the computational cost. The reasons are two fold: First, dense sampling in shots are needed to fully collapse the migration smiles due to the cross-spread acquisition geometry. Second, the stacking power objective function is very sensitive to the artifacts in the migration image, which could be translated into unrealistic model updates.

Process	Time/Shot (min)	# of Shots
Migration	7	3500
Gradient computation	30	3500 (1167)
Line search	21	3500

Table 1: Computational cost for each WEMVA iteration.

To demonstrate the redundancy of the shots when computing the gradients, we show the gradient in vertical velocity using all the shots in Figures 12(a). The gradient has been smoothed along the structure dips estimated from the initial anisotropic migration image. A fast velocity anomaly (indicated by the negative gradient) centered at $x = 9$km and $y = 15$km dominates the gradient.

The gradient using only a third of the shots is shown in Figures 13(a). Due to the reduced number of stacked shots, the amplitudes of the gradients are reduced. Nonetheless, the structures of the updates are remarkably similar except for minimal amplitude shifts. Therefore, we can safely reduce the number of shots in gradient computation without introducing significant errors. Similar comparisons and conclusions can be drawn for the gradients of ϵ and δ (Figures 12(b), 13(b), 12(c), and 13(c)).

We summarize the nonlinear conjugate gradient optimization workflow in Algorithm 2. With the shot reduction (shown between brackets in Table 1), we reduce the total time for one WEMVA iteration to 36 hours.

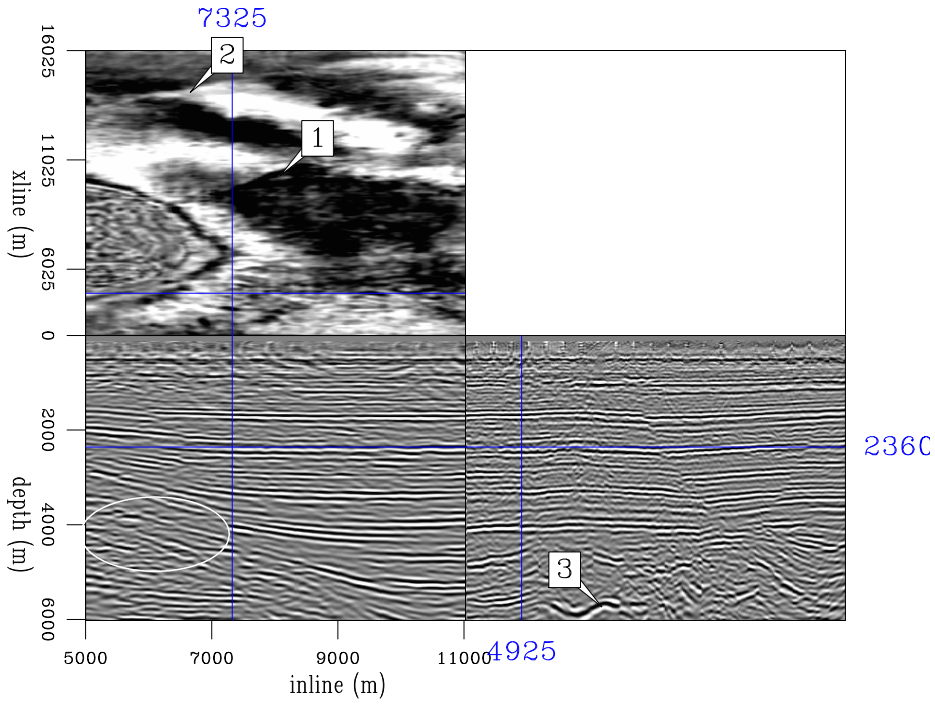

(a)

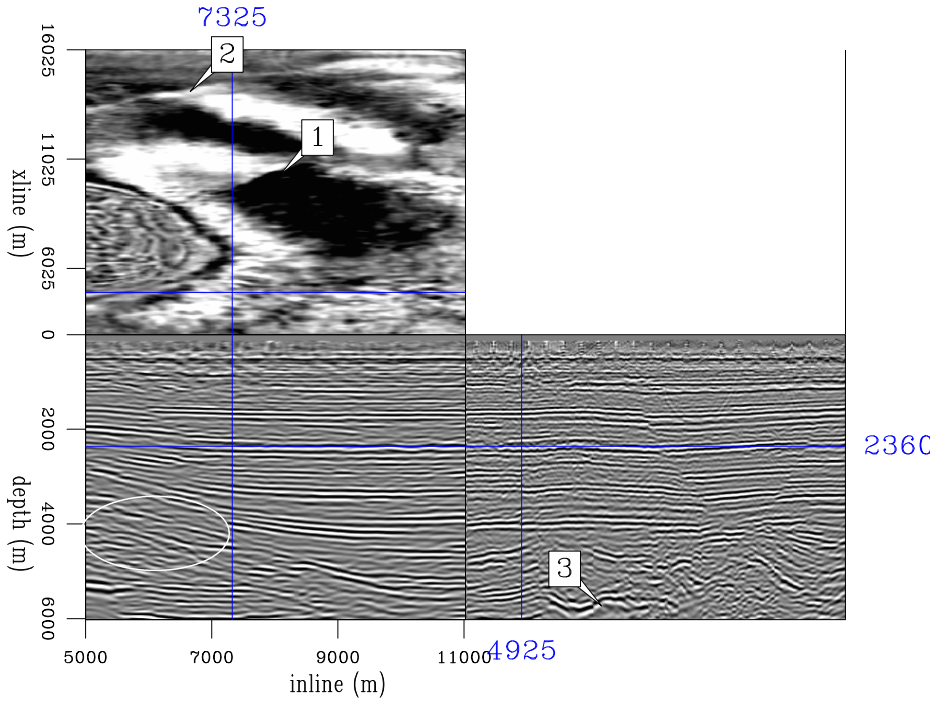

(b)

Figure 10: (a): Isotropic migration image using the isotropic velocity in Figure 9(a). (b): Anisotropic migration image using the models in Figure 9(b) to 9(d). [**CR**]

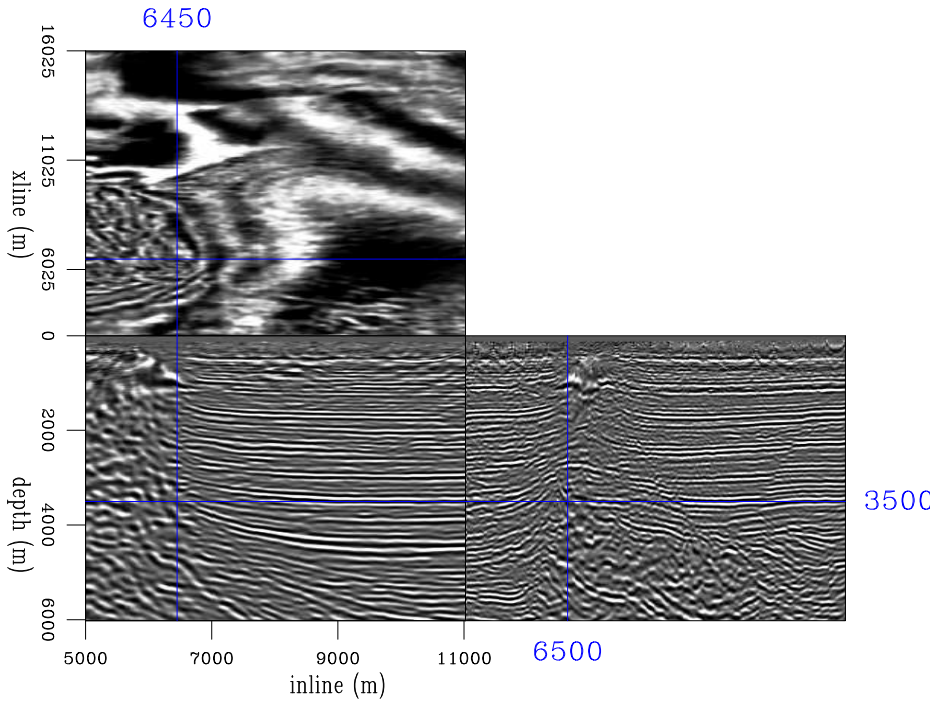

(a)

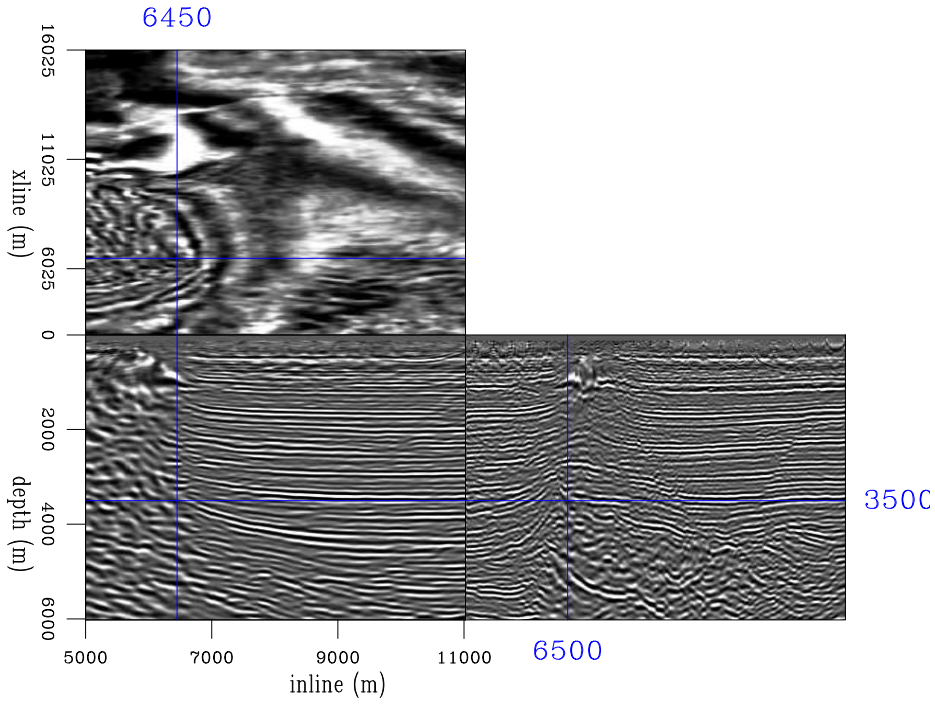

(b)

Figure 11: Same as Figure 10 but at a different location. [**CR**]

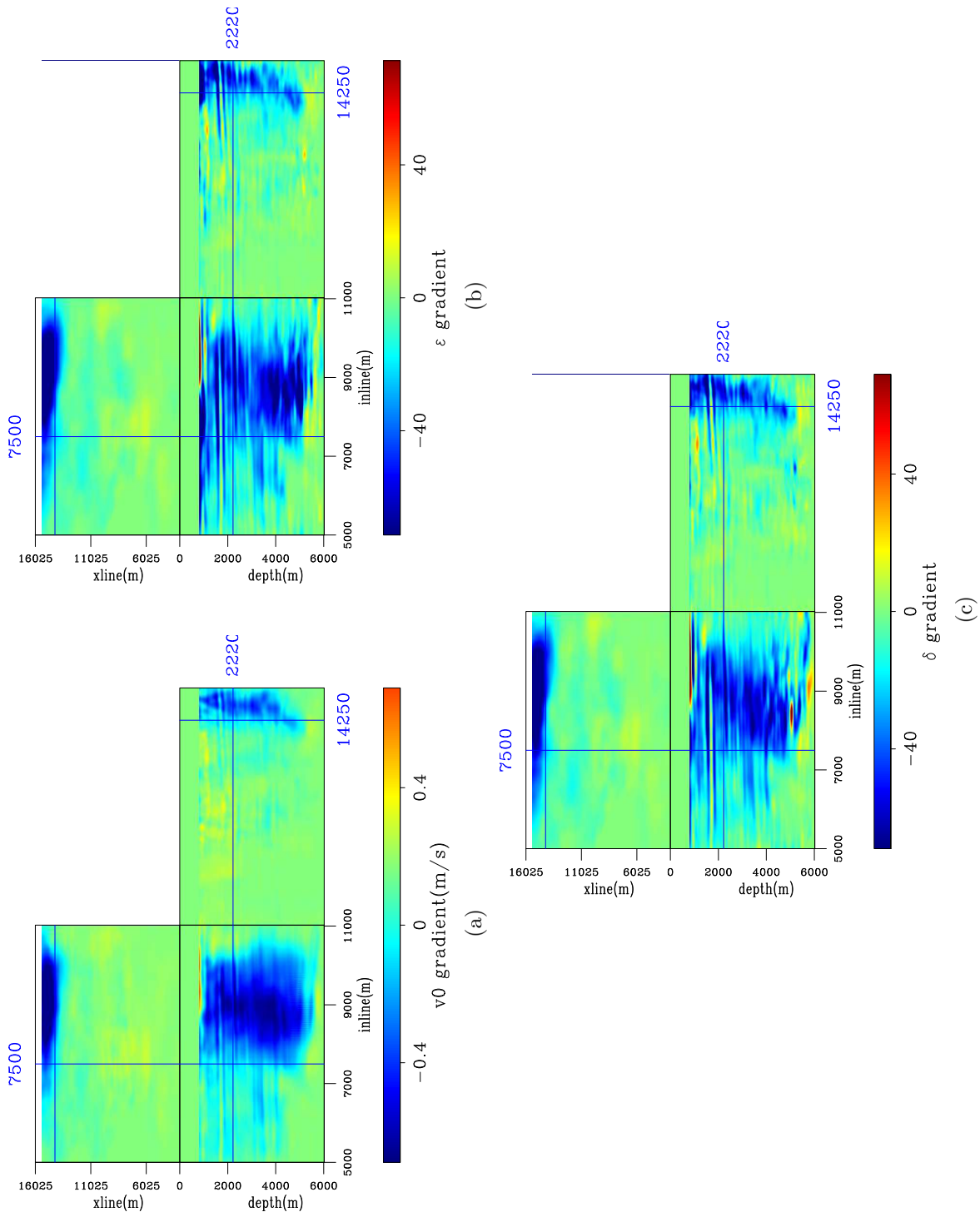

Figure 12: First anisotropic WEMVA gradient of (a) vertical velocity, (b) ϵ, and (c) δ using all shots. [**CR**]

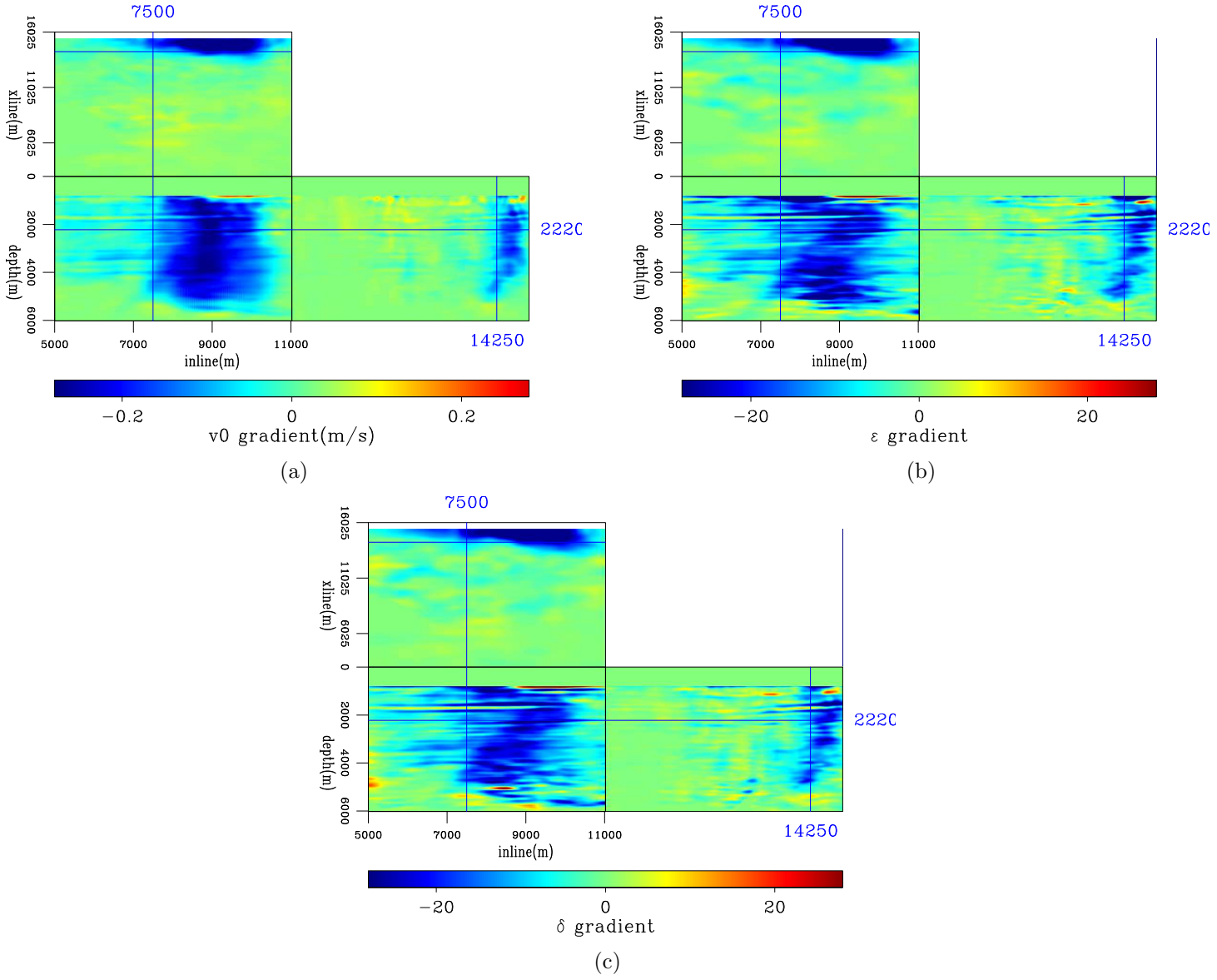

Figure 13: First anisotropic WEMVA gradient of (a) vertical velocity, (b) ϵ, and (c) δ using one-third of all the shots. [**CR**]

Algorithm 2 Optimization algorithm

initialize the model: $\mathbf{m}_0$
compute the migrated image: I_0
randomly select 1/3 of all shots
compute the gradient: $\mathbf{g}_0$
precondition the gradient: $\mathbf{g}_s^0 = \mathbf{S}\mathbf{\Sigma}\mathbf{\Sigma}^*\mathbf{S}^*\mathbf{g}_0$
initialize the search direction: $\mathbf{p}_0 = -\mathbf{g}_s^0$
for $k = 1 \cdots N_k$ **do**
  perform a line search: optimize λ, argmin $J(\mathbf{m}_{k-1} + \lambda \mathbf{p}_{k-1})$
  update the velocity model: $\mathbf{m}_k = \mathbf{m}_{k-1} + \lambda \mathbf{p}_{k-1}$
  compute the migrated image: I_k
  randomly select 1/3 of all shots
  compute the gradient: $\mathbf{g}_k$
  precondition the gradient: $\mathbf{g}_s^k = \mathbf{S}\mathbf{\Sigma}\mathbf{\Sigma}^*\mathbf{S}^*\mathbf{g}_k$
  find the search direction: $\mathbf{p}_k = -\mathbf{g}_k + \frac{(\mathbf{g}_s^k)^T(\mathbf{g}_s^k - \mathbf{g}_s^{k-1})}{(\mathbf{g}_s^{k-1})^T\mathbf{g}_s^{k-1}}$
end for

Compared with the gradient in vertical velocity (Figure 13(a)), the gradients in ϵ (Figure 13(b)) and δ (Figure 13(c)) show similar structures and point to the same update directions. These updates are determined by the WEMVA tomographic operator so that they increase the stacking power constructively. However, it is unrealistic for a shallow layer to have both high velocity and high anisotropy based on the lithological inversion results and our rock physics prior knowledge.

To honor the rock physics prior information, we apply the cross-parameter covariance matrix (Figures 3 and 4) in the preconditioning. As a result, the gradient direction in ϵ (Figure 14(b)) and δ (Figure 14(c)) in the shallow region has been reversed based on the negative correlation between velocity and anisotropy to follow the lithological assumptions. These preconditioned gradients (Figure 14) are used to perform line search and to update the background VTI model.

Preliminary inversion results

In this subsection, we present the preliminary inversion results after two nonlinear anisotropic WEMVA iterations. Figure 15 shows the updated VTI model. On average there are 5% positive updates in vertical velocity and 10% updates in both ϵ and δ at the strongest gradient location (Figure 14). We expect more balanced gradients once the anomaly in this region is properly updated.

Figure 16 compares the migration image with the initial model with the migration image with the updated model at a cross-line location where the model updates are strongest. On both in-line and cross-line section, the reflectors are better focused and more continuous as highlighted by the circles. On the depth slides, the resolution of the faults are much higher in the updated image.

Figure 17 compares the migration images where the model updates are not as strong. On the depth slice, the updated image has a better definition of the salt boundary. The reflectors in the in-line direction are more coherent (highlighted by the circles). As shown inside the circle on the cross-line section, the steeply dipping sediments pulled up by the salt body are much better imaged using the updated model. However, more iterations are needed to properly focus the incoherent events below 4km.

CONCLUSIONS

We tested our rock physics constrained anisotropic WEMVA method on a 3-D field data. Stochastic rock physics modeling provides a good initial anisotropic model. By constraining the anisotropic WEMVA with the geological and rock physics covariance, the inverted VTI model not only explains the reflection data, but also follows the basic geological and rock physics principles. The preliminary results after two iterations show promising improvements with better focusing for the shallow reflectors and better positioning for the steeply dipping reflectors. Further iterations are needed to improve the image below 4km.

ACKNOWLEDGEMENTS

The author thanks Schlumberger Multiclient for providing the field dataset. This paper includes data supplied by IHS Energy Log Services; Copyright (2013) IHS Energy Log Services Inc. I acknowledge the Stanford Center for Computational Earth and Environmental Science for providing computing resources.

REFERENCES

Bachrach, R., 2010, Applications of deterministic and stochastic rock physics modeling to anisotropic velocity model building: SEG Expanded Abstracts, **29**, 2436–2440.

Bandyopadhyay, K., 2009, Seismic anisotropy: geological causes and its implications: PhD thesis, Stanford University.

Li, Y. and B. Biondi, 2011, Migration velocity analysis for anisotropic models: SEG Expanded Abstract, **30**, 201–206.

Li, Y. E., B. Biondi, D. Nichols, G. Mavko, and R. Clapp, 2013, Stochastic rock physics modeling for seismic anisotropy: SEP-Report, **149**, 289–306.

Li, Y. E., R. Clapp, B. Biondi, and D. Nichols, 2014, Rock physics constrained anisotropic WEMVA: Part I - Theory and synthetic test : SEP-Report, **152**, 61–94.

Shan, G., 2008, Imaging of steep reflectors in anisotropic media by wavefield extrapolation: PhD thesis, Stanford University.

Vernik, L. and X. Liu, 1997, Velocity anisotropy of shales: A petrophysical study: Geophysics, **62**, 521–532.

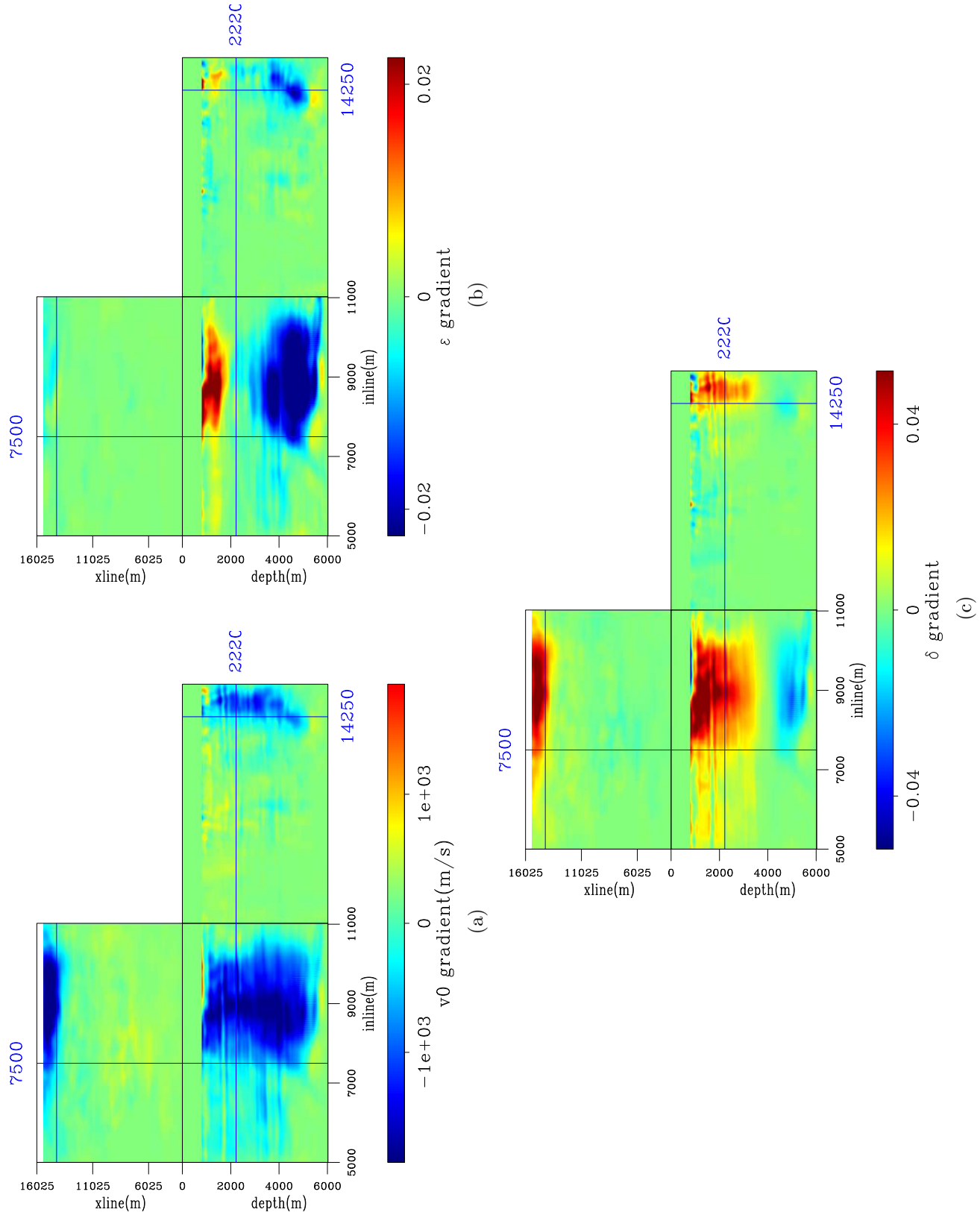

Figure 14: First anisotropic WEMVA gradient of (a) vertical velocity, (b) ϵ, and (c) δ using one-third of all the shots. **[CR]**

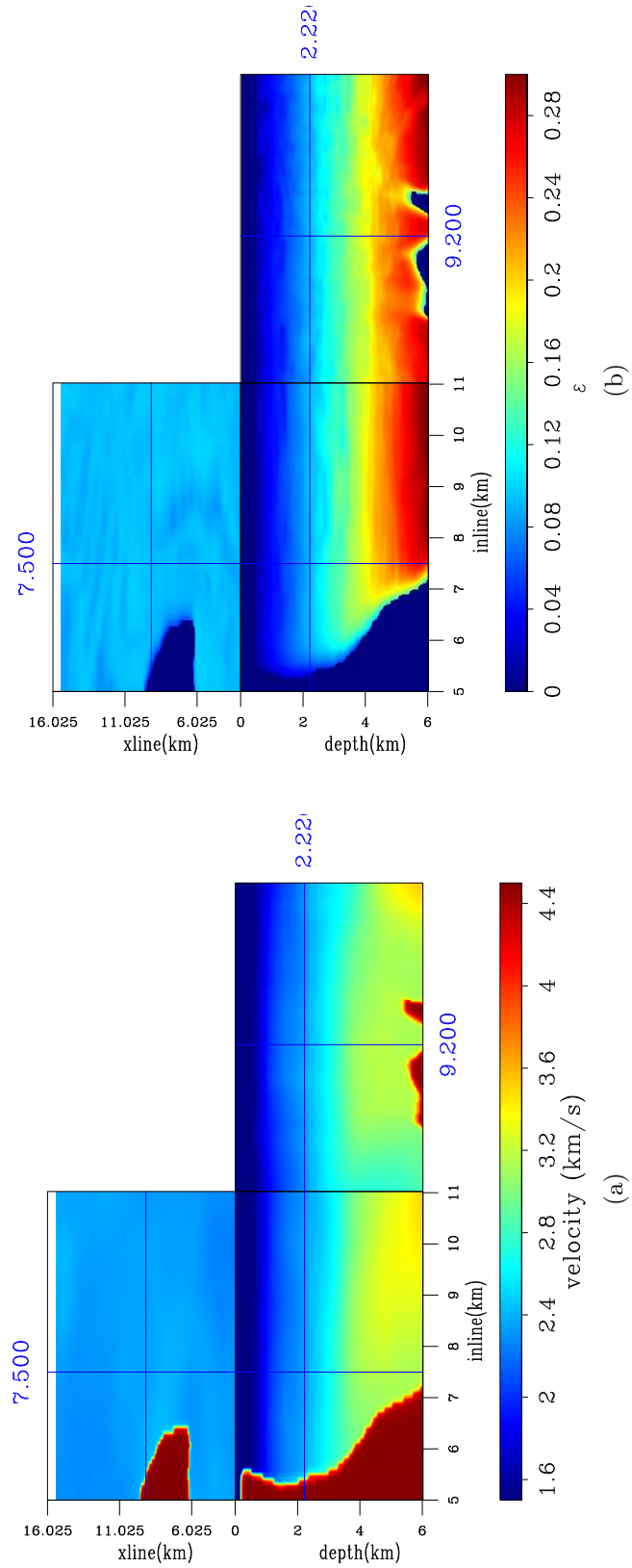

Figure 15: (a): Vertical velocity model, (b): ϵ model and (c): δ model after two anisotropic WEMVA iterations. [**CR**]

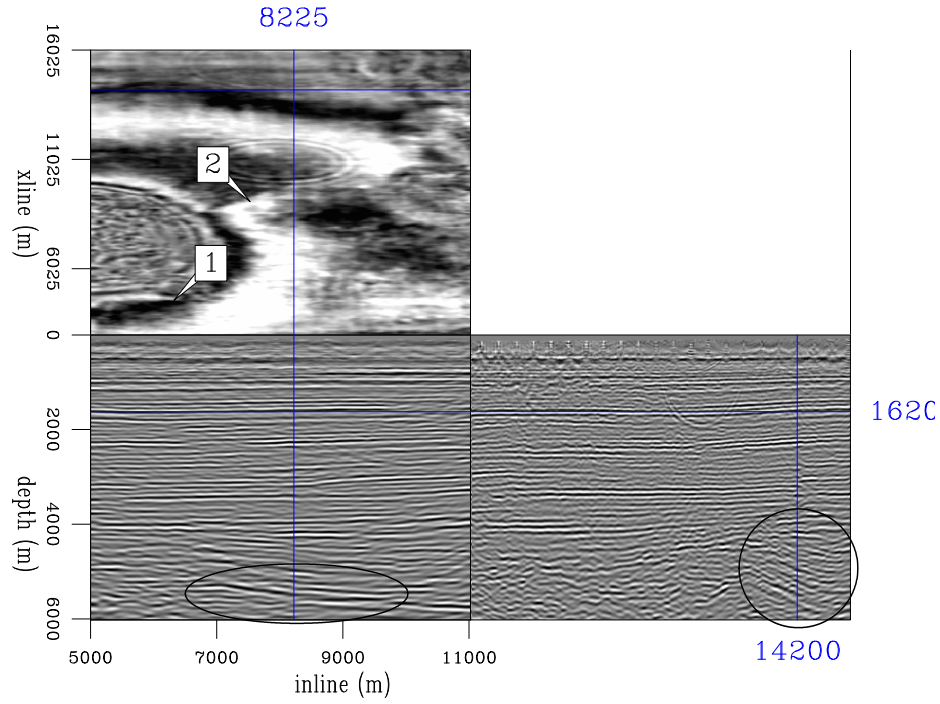

(a)

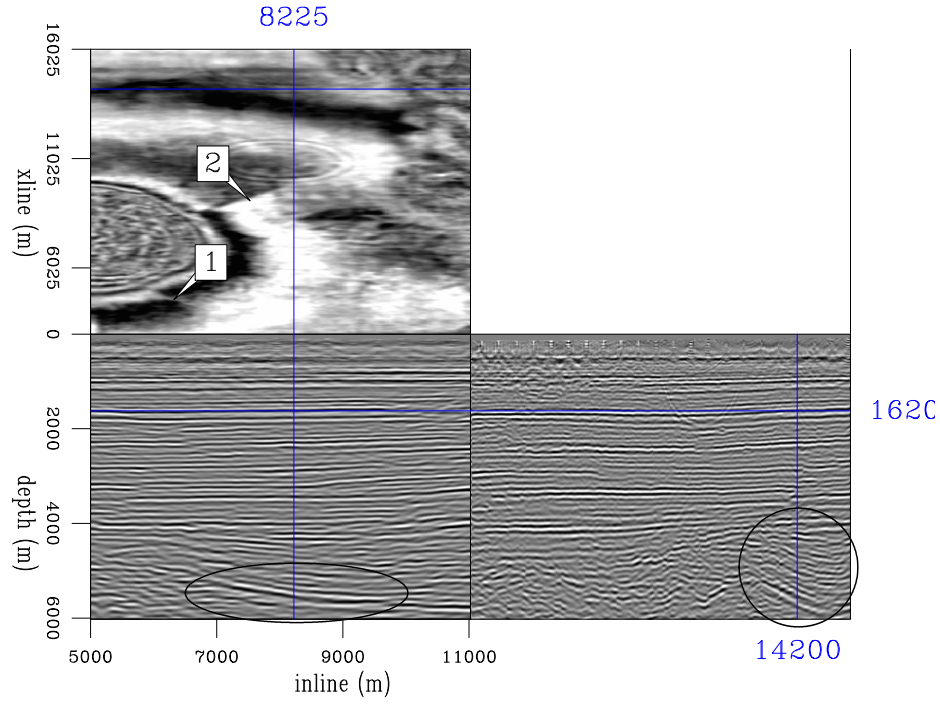

(b)

Figure 16: (a) Migration image using the initial anisotropic model. (b) Migration image using the updated anisotropic model after 2 iterations. Flags 1 and 2 point out two faults which are better imaged in the depth slice with the updated model. Reflectors in both circles are more continuous in (b). [**CR**]

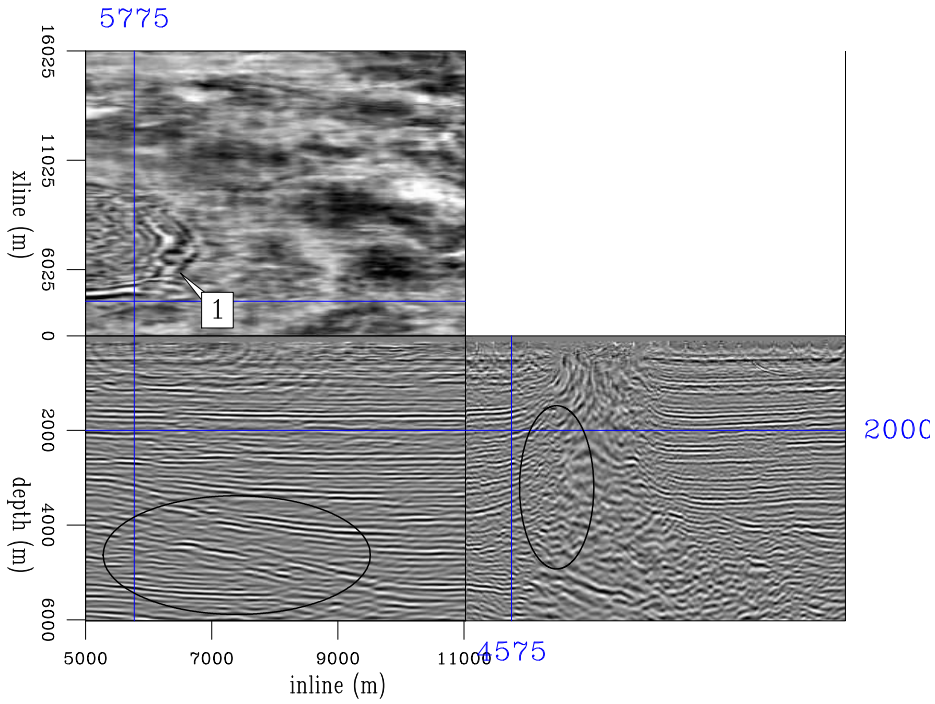

(a)

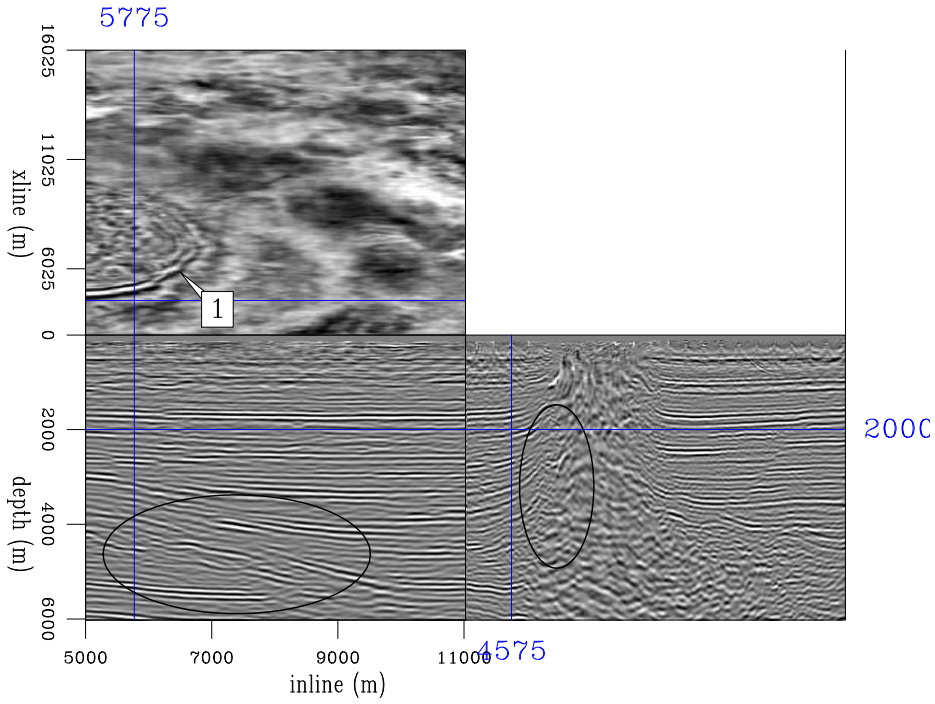

(b)

Figure 17: Same as Figure 17 but at a different location. Flag 1 points out the much higher resolution salt boundary in (b). The reflections in the circle on the in-line section are more continuous. The steeply dipping reflectors highlighted by the circle in the cross-line direction are much better imaged in (b). [**CR**]